minerals

MDPI

Article

Petrogenesis of Early Cretaceous High-Mg Adakitic Pluton in the North Lhasa Block, Tibet Plateau: Implications for the Tethyan Orogeny

Qian-Ru Xiao [1], Yong-Feng Wei [1,2,*], Zhong-Yuan Liu [1], Fu-Hao Xiong [1], Lei Fan [1], Jian-Xin Wu [1] and Han Zhao [1]

[1] College of Earth Sciences, Chengdu University of Technology, Chengdu 610059, China; xiaoqianru@cdut.edu.cn (Q.-R.X.); Liuzhongyuan43@hotmail.com (Z.-Y.L.); xiongfuhao2014@cdut.edu.cn (F.-H.X.); fanl.vra@foxmail.com (L.F.); wujianxin34@hotmail.com (J.-X.W.); zhaohan2013@cdut.edu.cn (H.Z.)

[2] Regional Geological Survey Team, Sichuan Geology and Mineral Bureau, Shuangliu 610213, China

* Correspondence: weiyongfeng1900@hotmail.com

Abstract: Late Mesozoic igneous rocks from the north Lhasa block record the Neo-Tethyan orogeny in the southern Tibet Plateau. This study presents geochronological and geochemical data of Bieruozecuo quartz diorite pluton in the northern margin of the Lhasa block to constrain its petrogenesis and tectonic implications. The LA–ICP–MS zircon U–Pb geochronology of quartz diorites shows that the emplacement occurs at ca. 114–116 Ma, belonging to the products of Early Cretaceous magmatic activities. The high concentrations of TiO_2, MgO, and MnO, together with SiO_2 vs. K_2O and A/NK vs. A/CNK diagrams, all suggest that the Bieruozecuo quartz diorites are meta-aluminous and high-potassium calc-alkaline rocks. Their high Sr and low Y and Yb contents, as well as high Sr/Y and La/Yb ratios, are consistent with the typical adakitic rocks. The REE patterns show a large distribution of compositions, which have LREE, while HREE are buffered, along with large ratios of $(La/Yb)_N$, as well as high values of K_2O/Na_2O, Mg#, Cr, and Ni, all of which imply the partial melting of a delaminated lower crust, without obvious fractional crystallization during the magma ascending and emplacement. This study suggests that, with the closure of the Bangonghu–Nujiang Tethys Ocean Basin, the post-collisional extension of the north Lhasa block will have started no later than ca. 114–116 Ma. Combined with the previous studies, our new data demonstrates that the partial melting of the delaminated lower crust, in a post-collisional setting, may be the main mechanism responsible for the ca. 116–82 Ma adakitic magmatism in the north Lhasa block.

Keywords: Lhasa block; neo-tethyan orogeny; cretaceous; adakite; petrogenesis; tectonic setting

Citation: Xiao, Q.-R.; Wei, Y.-F.; Liu, Z.-Y.; Xiong, F.-H.; Fan, L.; Wu, J.-X.; Zhao, H. Petrogenesis of Early Cretaceous High-Mg Adakitic Pluton in the North Lhasa Block, Tibet Plateau: Implications for the Tethyan Orogeny. *Minerals* **2022**, *12*, 213. https://doi.org/10.3390/min12020213

Academic Editors: Sergei Khromykh and Andrei Tsygankov

Received: 12 December 2021
Accepted: 3 February 2022
Published: 7 February 2022

1. Introduction

The Lhasa block in the southern Tibet Plateau is characterized by the presence of large-scale Late Mesozoic–Cenozoic magmatic rocks, which records the magmatic–tectonic evolution and geodynamic processes during the oceanic lithosphere subduction and collision/accretion of terranes [1–6]. Hence, unraveling their petrogenesis is the key to understanding the tectonic evolution and Neo-Tethyan orogeny. Despite many studies that have been carried out on the Late Mesozoic magmatic rocks in the Lhasa block, the models, proposed so far on their petrogenesis and dynamic background, are still controversial. Some studies propose that the Late Mesozoic magmatic activity in the Lhasa block was formed during the northward subduction of the southern Yarlung Zangbo Neo-Tethyan -oceanic slab [4,7,8]. In contrast, others believe that their petrogenesis is closely related to the southward oceanic lithosphere subduction or terrane collision during the Northern Bangong Hu-Nujiang Tethys orogeny [2,3,9,10]. Meanwhile, previously published studies on the magma source of Late Mesozoic magmatic rocks in the Lhasa block are not consistent, suggesting different models, including remelting of the thickened lower crust in a

collisional setting [7] and partial melting of Neo-Tethyan oceanic crust [2]. Therefore, it is necessary to continue to study the petrogenesis and tectonic setting of the Late Mesozoic magmatic rocks in the Lhasa block, to get a better understanding the Neo-Tethyan orogeny.

In this contribution, we present studies on the petrology, petrography, LA–ICP–MS zircon U–Pb chronology, and whole-rock geochemistry of one Early Cretaceous quartz diorite pluton in the northern Lhasa block. Combined with published data of the other Late Mesozoic coeval magmatic rocks in northern and central Tibet, we discuss the melt sources and magmatic evolution processes, as well as their tectonic implications on the Neo-Tethyan orogeny in the Lhasa block, southern Tibet.

2. Geological Setting and Petrography

The Tibet Plateau, located in the eastern part of the Tethys tectonic domain, is a key area for studying the geodynamic processes of oceanic lithosphere subduction and collision of the Tethys terranes. Multiple Tethyan subductions and accretion orogenic processes occurred in Tibet Plateau, including the Early Paleozoic Proto-Tethys, Carboniferous–Triassic Paleo-Tethys, and Mesozoic–Cenozoic Neo-Tethys orogenies [11–15]. The Lhasa block is located in the southern Tibet Plateau, which is bound by the Yarlung Zangbo Neo-Tethyan Tethyan suture zone (IYZSZ) to the south and northern Bangonghu–Nujiang suture zone (BNSZ) to the north. Taking the Lobadui Milashan fault (LMF) and Shiquanhe-Namucuo ophiolite melange belt (SNMZ) as the boundaries, the Lhasa block is subdivided into the north Lhasa block (NL), central Lhasa block (CL), and south Lhasa block (SL) (Figure 1a). Mesozoic and Cenozoic magmatic rocks are the dominant rocks in the entire Lhasa block. Triassic–Cretaceous magmatic rocks, forming a large-scale Gandeses batholith belt, occur as the dominant rocks, only in the south Lhasa block, whereas the Late Jurassic/Early Cretaceous sedimentary strata, Zenong Group volcanic rocks, and Early Cretaceous intrusive rocks are widely exposed in the central and north Lhasa blocks [8,16,17] (Figure 1b).

The Bieruozecuo quartz diorite pluton is located in the transitional part of the central and north Lhasa blocks. This area is characterized by the development of Jurassic–Cretaceous volcanic sedimentary strata and a large number of intermediate-acid intrusive rocks (Figure 1b). The Early Cretaceous Bieruozecuo quartz diorite pluton is irregular or nearly oval in form, emplaced into the Early Cretaceous Shishenla and Duoni formations, with the acreage for a single mass rock of 10–25 km^2. The investigated intrusion is about 19 km^2. The petrographic observation of the outer rim of the pluton provides good evidence for the thermal contact metamorphism, including hornfelsification, silicification, and marbleization. The quartz diorite is a greyish–green color and displays a fine-grained texture. Plagioclase (~50%) is the most abundant mineral, followed by alkaline feldspar (~18%), quartz (~15%), hornblende (~9%), and biotite (~4%). The plagioclase group of minerals consists of oligoclase and andesine, in the form of subhedral crystals, with a diameter of 0.5–1.6 mm. The euhedral growth zoning was generally observed in andesine. The main variety of alkaline feldspar is orthoclase. Most of the orthoclase grains are subhedral to anhedral. The quartz is heteromorphic. Alkali feldspar has xenomorphic granular structure. Zircon, apatite, magnetite, and sphene are rare, and other minerals are present only in trace amounts (Figure 2). The alterations cannot be observed in the fresh, thin sections of the samples.

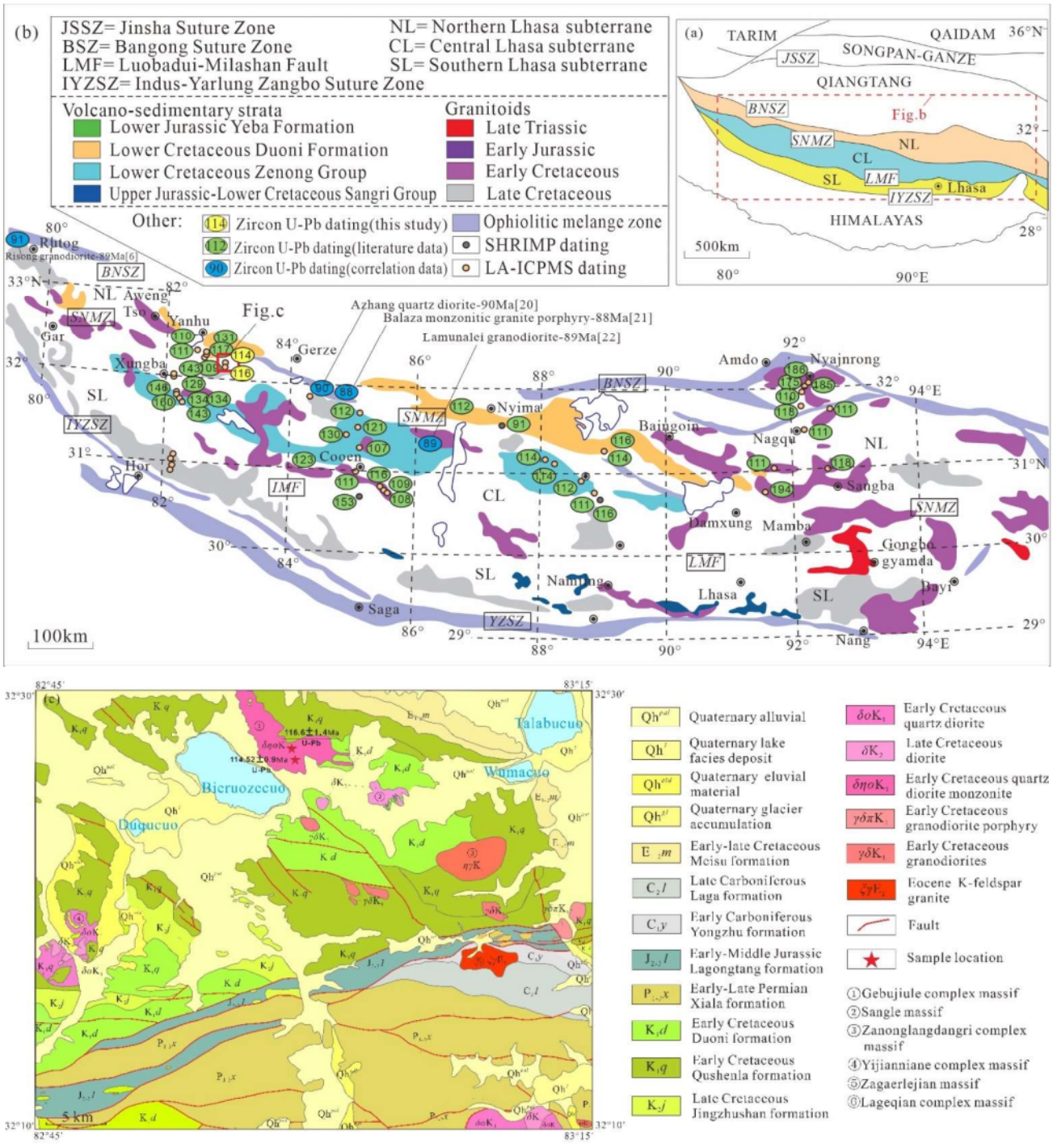

Figure 1. (**a**) Schematic tectonic framework of the Tibetan Plateau (modified from [18]); (**b**) tectonic framework of the Lhasa terrane, showing major tectonic subdivisions (modified from [19]; the correlation data are from [6,20–22]); (**c**) simplified geological map showing sample locations.

Figure 2. (**a**) Field photograph showing the outcrops of Bieruozecuo quartz diorite adakitic rocks; (**b**) Microphotograph of the adakitic rock (sample P10-19); (**c**) Microphotograph of the adakitic rock (sample P11-6). Qtz = quartz; Pl = plagioclase; Afs = alkali feldspar; Bt = biotite; Hbl = hornblende; Mag = magnetite; Ap = apatite; Zrn = zircon; Chl = chlorite; Spn = sphene.

3. Samples and Methods

Two samples of the Bieruozecuo quartz diorite were collected for zircon geochronology analysis, and sample P11(20) was collected from the inner of the pluton (82°55′41″ E, 32°20′04″ N), while sample P11(46) was collected from the rim of the pluton (82°56′22″ E, 32°19′53″ N). Prior to LA–ICP–MS analyses, the samples were pretreated, crushed, and sorted at the Huayang Rock and Mineral Testing Center of Sichuan, China. Zircon concentrates were mounted in epoxy mounts, which were then carefully polished. All zircon grains were observed under a microscope, with transmitted and reflected light, as well as with cathodoluminescence (CL) imaging to confirm high transparency and avoid measuring spots with inclusions or/and cracks. Measurements of U and Pb isotopes were carried out using LA–ICP–MS, equipped with an ArF 193 nm UV excimer laser, at the State Key Laboratory of Dynamics, Northwestern University, China. The single pulse energy was set

to 220 mJ, and the maximum laser repetition rate was 20 Hz. A fluence of 50 Jcm^{-2} was chosen, with a beam diameter of around 60 µm. The standard zircon 91500 was used as an external standard for the calibration of the Pb–U. For quality assurance, the standard was analyzed at the end of the analytical run, after the measurement of six samples. Further data evaluation has been performed by using ISOPLOT and SQUID software. More detailed analytical procedures are described by [23].

The bulk compositions (major, trace, and rare earth elements) of samples were performed using an Axios X-ray fluorescence spectrometer, X Series 2 plasma-mass spectrometer, IRIS Intripid2XSP ICP full spectrum direct-reading spectrometer, zeenit600 graphite furnace atomic absorption spectrometer, and AFS-230E atomic fluorescence spectrometer at Zhongnan Mineral Resources Supervision and Testing Center. The analytical uncertainties were less than 5%.

4. Results

4.1. U–Pb Zircon Age

U–Pb zircon data are shown in Table 1. Zircon grains from sample P11(20) and sample P11(46) are mostly euhedral to subhedral and 95 to 220 µm in length. The zircons in the two samples show similar zircon texture; both the inherited cores and magmatic rims of the zircons were observed in the two studied samples. Most zircon grains are transparent and show euhedral concentric zoning under CL images (Figure 3). A total of 48 analyses of zircon grains were obtained (Table 1). The concordance curves of the quartz diorite in sample P11(20) are shown in Figure 4a. The concordant age within analytical errors is 114.36.1 ± 0.43 Ma (MSWD = 0.44), yielding a weighted mean $^{206}Pb/^{238}U$ age of 114.52 ± 0.91 Ma (mean squared weighted deviation (MSWD) = 0.87). The concordance age of zircons in sample P11(46) is shown in Figure 4b, and its concordance age is 116.7 ± 0.70 Ma (MSWD =7.7), with a weighted mean $^{206}Pb/^{238}U$ age of 116.6 ± 1.4 Ma (MSWD = 0.95). Therefore, the crystallization age of the Bieruozecuo quartz diorite is 116 ~ 114 Ma (Early Cretaceous).

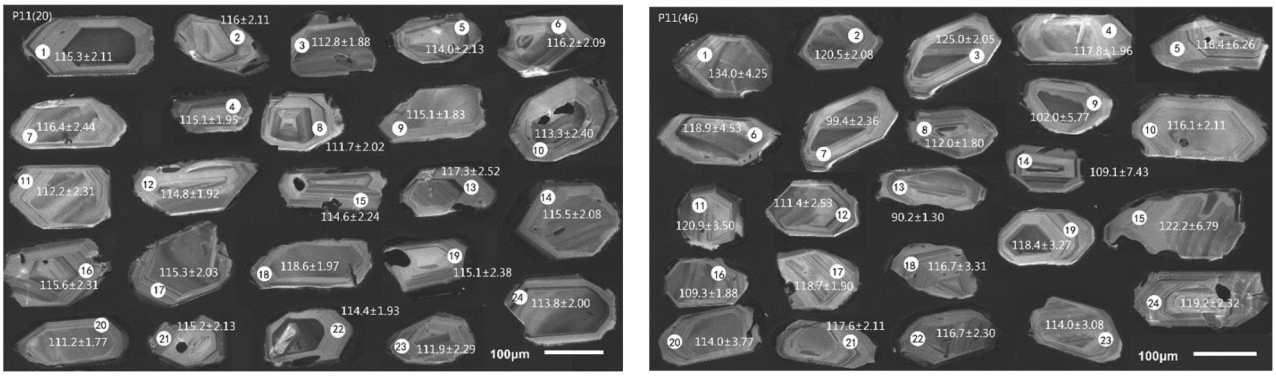

(**a**) (**b**)

Figure 3. Representative cathodoluminescence images of zircon grains, analyzed from (**a**) sample 11(20) and (**b**) sample 11(46).

Table 1. LA–ICP–MS zircon U–Pb ages for samples from the Bieruozecuo pluton in the Lhasa block, southern Tibet.

Sample Mark	Isotope Ratio								Age (Ma)							
	$^{207}Pb/^{206}Pb$		$^{207}Pb/^{235}U$		$^{206}Pb/^{238}U$		$^{208}Pb/^{232}Th$		$^{207}Pb/^{206}Pb$		$^{207}Pb/^{235}U$		$^{206}Pb/^{238}U$		$^{208}Pb/^{232}Th$	
	Ratio	1σ	Ratio	1σ	Ratio	1σ	Ratio	1σ	Age	1σ	Age	1σ	Age	1σ	Age	1σ
P11(20)-01	0.047 09	0.003 66	0.117 23	0.008 38	0.018 05	0.000 33	0.005 58	0.000 21	53.3	176.17	112.6	7.62	115.3	2.11	112.4	4.28
P11(20)-02	0.054 60	0.003 84	0.136 79	0.008 67	0.018 16	0.000 33	0.006 13	0.000 25	395.9	150.5	130.2	7.75	116	2.11	123.5	4.95
P11(20)-03	0.046 15	0.002 95	0.112 35	0.006 34	0.017 65	0.000 30	0.005 62	0.000 17	5.7	146.94	108.1	5.79	112.8	1.88	113.3	3.48
P11(20)-04	0.050 72	0.003 13	0.126 03	0.006 82	0.018 02	0.000 31	0.005 62	0.000 18	228.3	136.7	120.5	6.15	115.1	1.95	113.3	3.66
P11(20)-05	0.050 27	0.003 95	0.123 74	0.008 95	0.017 85	0.000 34	0.005 72	0.000 23	207.3	172.58	118.5	8.09	114	2.13	115.3	4.53
P11(20)-06	0.050 35	0.003 54	0.126 34	0.008 00	0.018 19	0.000 33	0.005 80	0.000 21	211.2	154.95	120.8	7.21	116.2	2.09	117	4.12
P11(20)-07	0.049 35	0.004 74	0.123 99	0.011 23	0.018 22	0.000 39	0.006 14	0.000 28	164.5	210.23	118.7	10.15	116.4	2.44	123.7	5.67
P11(20)-08	0.047 21	0.003 48	0.113 80	0.007 64	0.017 48	0.000 32	0.005 84	0.000 19	59.5	167.44	109.4	6.97	111.7	2.02	117.7	3.88
P11(20)-09	0.045 39	0.002 65	0.112 80	0.005 68	0.018 02	0.000 29	0.005 79	0.000 14	0.1	101.05	108.5	5.18	115.1	1.83	116.7	2.84
P11(20)-10	0.040 63	0.004 97	0.099 35	0.011 72	0.017 73	0.000 38	0.005 53	0.000 28	0.1	0	96.2	10.83	113.3	2.4	111.5	5.68
P11(20)-11	0.045 52	0.004 49	0.110 21	0.010 28	0.017 56	0.000 36	0.005 60	0.000 25	0.1	194.99	106.2	9.4	112.2	2.31	112.9	4.95
P11(20)-12	0.050 94	0.003 09	0.126 26	0.006 67	0.017 97	0.000 30	0.006 00	0.000 16	237.9	134.15	120.7	6.02	114.8	1.92	121	3.16
P11(20)-13	0.052 85	0.005 32	0.133 82	0.012 75	0.018 36	0.000 40	0.006 24	0.000 31	322.4	213.24	127.5	11.42	117.3	2.52	125.7	6.26
P11(20)-14	0.053 41	0.003 64	0.133 11	0.008 10	0.018 07	0.000 33	0.006 16	0.000 20	346.1	146.56	126.9	7.26	115.5	2.08	124.2	3.93
P11(20)-15	0.058 74	0.004 54	0.145 32	0.010 28	0.017 94	0.000 35	0.006 72	0.000 26	557.4	160.27	137.8	9.11	114.6	2.24	135.4	5.28
P11(20)-16	0.044 40	0.004 30	0.110 74	0.010 15	0.018 09	0.000 36	0.006 04	0.000 26	0.1	133.26	106.6	9.28	115.6	2.31	121.8	5.31
P11(20)-17	0.047 58	0.003 48	0.118 39	0.007 87	0.018 04	0.000 32	0.005 92	0.000 18	77.7	165.72	113.6	7.15	115.3	2.03	119.3	3.7
P11(20)-18	0.049 51	0.003 06	0.126 83	0.006 86	0.018 57	0.000 31	0.006 11	0.000 17	172.2	138.15	121.2	6.18	118.6	1.97	123	3.5
P11(20)-19	0.051 66	0.004 69	0.128 32	0.010 89	0.018 01	0.000 38	0.006 02	0.000 26	270.5	194.89	122.6	9.8	115.1	2.38	121.3	5.24
P11(20)-20	0.049 22	0.002 84	0.118 16	0.005 86	0.017 41	0.000 28	0.005 84	0.000 14	158.5	129.68	113.4	5.32	111.2	1.77	117.6	2.82
P11(20)-21	0.063 05	0.004 17	0.156 74	0.009 17	0.018 03	0.000 34	0.006 21	0.000 23	709.8	134.61	147.8	8.05	115.2	2.13	125.1	4.61
P11(20)-22	0.047 64	0.003 13	0.117 60	0.006 88	0.017 90	0.000 31	0.005 94	0.000 19	80.8	149.81	112.9	6.25	114.4	1.93	119.7	3.73
P11(20)-23	0.049 29	0.004 50	0.119 04	0.010 18	0.017 51	0.000 36	0.005 84	0.000 25	161.7	200.42	114.2	9.24	111.9	2.29	117.6	4.99
P11(20)-24	0.050 00	0.003 52	0.122 78	0.007 81	0.017 80	0.000 32	0.005 95	0.000 21	195.2	155.96	117.6	7.06	113.8	2	119.9	4.16
P11(46)-01	0.050 93	0.007 32	0.147 50	0.020 37	0.021 00	0.000 67	0.007 45	0.000 52	237.5	300.97	139.7	18.02	134	4.25	149.9	10.35
P11(46)-02	0.050 78	0.003 63	0.132 11	0.008 44	0.018 87	0.000 33	0.006 60	0.000 21	230.9	157.24	126	7.57	120.5	2.08	132.9	4.21
P11(46)-03	0.051 30	0.00358	0.138 46	0.008 61	0.019 57	0.000 32	0.006 73	0.000 22	254.2	152.94	131.7	7.68	125	2.05	135.5	4.49
P11(46)-04	0.051 82	0.00352	0.131 82	0.007 93	0.018 45	0.000 31	0.006 49	0.000 21	277.4	148.45	125.7	7.11	117.8	1.96	130.8	4.18
P11(46)-05	0.049 36	0.01251	0.124 03	0.030 65	0.018 22	0.000 99	0.008 50	0.000 90	164.7	504.78	118.7	27.69	116.4	6.26	171	17.94

Table 1. *Cont.*

Sample Mark	Isotope Ratio								Age (Ma)							
	$^{207}Pb/^{206}Pb$		$^{207}Pb/^{235}U$		$^{206}Pb/^{238}U$		$^{208}Pb/^{232}Th$		$^{207}Pb/^{206}Pb$		$^{207}Pb/^{235}U$		$^{206}Pb/^{238}U$		$^{208}Pb/^{232}Th$	
	Ratio	1σ	Ratio	1σ	Ratio	1σ	Ratio	1σ	Age	1σ	Age	1σ	Age	1σ	Age	1σ
P11(46)-06	0.052 30	0.00907	0.134 26	0.022 51	0.018 61	0.000 72	0.006 21	0.000 57	298.7	353.77	127.9	20.15	118.9	4.53	125.1	11.44
P11(46)-07	0.047 86	0.00684	0.102 52	0.014 19	0.015 53	0.000 37	0.005 29	0.000 33	91.2	308.93	99.1	13.07	99.4	2.36	106.7	6.7
P11(46)-08	0.049 22	0.00339	0.118 91	0.007 28	0.017 52	0.000 28	0.005 74	0.000 19	158.2	153.49	114.1	6.6	112	1.8	115.6	3.78
P11(46)-09	0.049 35	0.01375	0.108 52	0.029 54	0.015 94	0.000 91	0.005 96	0.000 62	164.4	547.07	104.6	27.06	102	5.77	120.1	12.4
P11(46)-10	0.051 10	0.00404	0.128 08	0.009 25	0.018 18	0.000 33	0.006 27	0.000 24	245.2	172.54	122.4	8.33	116.1	2.11	126.2	4.86
P11(46)-11	0.049 24	0.00643	0.128 54	0.016 04	0.018 93	0.000 55	0.006 00	0.000 41	159.2	279.47	122.8	14.43	120.9	3.5	120.9	8.28
P11(46)-12	0.050 22	0.00528	0.120 70	0.011 98	0.017 43	0.000 40	0.006 35	0.000 31	205	226.96	115.7	10.86	111.4	2.53	128	6.28
P11(46)-13	0.146 93	0.00607	0.285 55	0.007 94	0.014 09	0.000 20	0.009 60	0.000 17	2310.5	69.22	255.1	6.27	90.2	1.3	193.1	3.47
P11(46)-14	0.053 17	0.01613	0.125 22	0.037 02	0.017 08	0.001 17	0.006 53	0.001 06	336	571.83	119.8	33.41	109.1	7.43	131.5	21.25
P11(46)-15	0.051 18	0.01302	0.135 07	0.033 48	0.019 14	0.001 07	0.009 30	0.001 09	248.8	499.44	128.6	29.95	122.2	6.79	187.1	21.76
P11(46)-16	0.052 42	0.00385	0.123 60	0.008 19	0.017 10	0.000 30	0.005 50	0.000 16	303.7	158.38	118.3	7.4	109.3	1.88	110.9	3.27
P11(46)-17	0.050 34	0.00342	0.129 04	0.007 80	0.018 59	0.000 30	0.006 82	0.000 21	210.9	150.2	123.2	7.02	118.7	1.9	137.4	4.25
P11(46)-18	0.051 45	0.00644	0.129 66	0.015 46	0.018 27	0.000 52	0.007 33	0.000 44	261.1	264.1	123.8	13.9	116.7	3.31	147.7	8.92
P11(46)-19	0.052 68	0.00621	0.134 72	0.015 08	0.018 54	0.000 52	0.006 12	0.000 40	315	248.02	128.3	13.49	118.4	3.27	123.4	7.95
P11(46)-20	0.053 05	0.00772	0.130 47	0.018 24	0.017 83	0.000 60	0.007 22	0.000 52	330.8	300.38	124.5	16.38	114	3.77	145.4	10.49
P11(46)-21	0.052 13	0.00377	0.132 38	0.008 59	0.018 41	0.000 33	0.005 79	0.000 19	291.2	156.78	126.2	7.7	117.6	2.11	116.7	3.81
P11(46)-22	0.052 02	0.00425	0.131 05	0.009 82	0.018 27	0.000 36	0.005 97	0.000 21	286.3	176.06	125	8.82	116.7	2.3	120.3	4.19
P11(46)-23	0.050 78	0.00602	0.124 97	0.014 08	0.017 85	0.000 49	0.005 76	0.000 30	230.7	252.21	119.6	12.71	114	3.08	116.1	6.1
P11(46)-24	0.051 74	0.00463	0.133 14	0.011 10	0.018 66	0.000 37	0.006 27	0.000 24	274.1	192.25	126.9	9.95	119.2	2.32	126.4	4.89

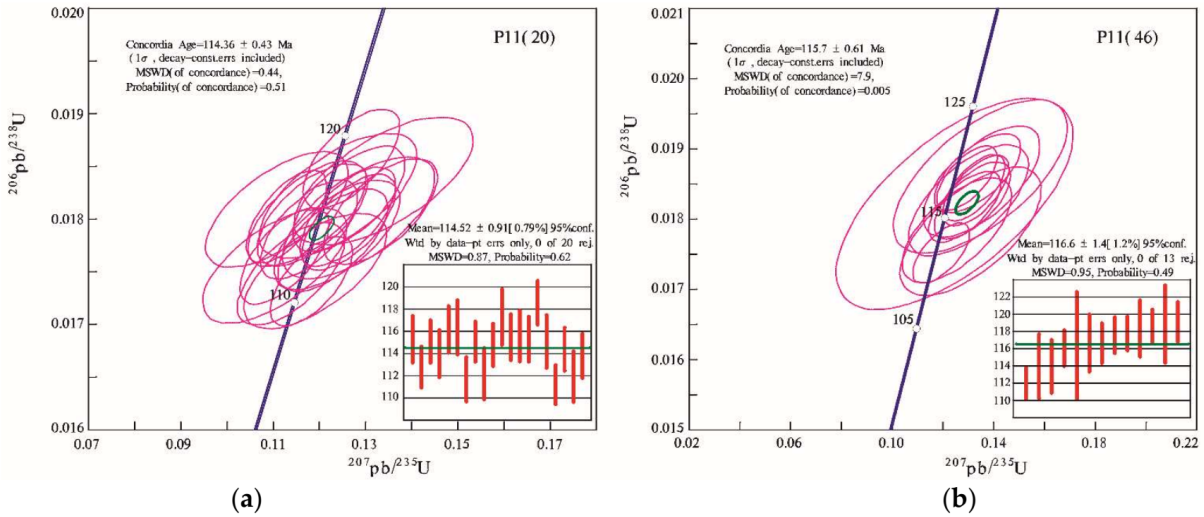

Figure 4. Concordia diagram for zircons from the samples; the circles indicate the locations of LA–ICP–MS U–Pb dating spot analyses. (**a**) P11(20); (**b**) P11(46).

4.2. Bulk Geochemical Characteristics

The major and trace element compositions of the representative samples (N = 15) from the Bieruozecuo pluton are presented in Table 2. The studied samples have low contents of LOI, indicating that the samples are fresh, and the geochemical data can be used to efficiently constain their petregenesis. They contain higher Al_2O_3 (14.72–15.75 wt.%), and Na_2O (3.27–4.02 wt.%), but the lower concentrations of MgO (1.60–2.67 wt.%) and TiO_2 (0.45–0.71 wt.%). ALK, Na_2O/K_2O ratios, and A/CNK ratios are 6.50–7.26%, 0.95–1.49, 0.89–0.93, respectively. The studied rocks show high-K calc-alkaline affinity (Figure 5a) and fall into the meta-aluminous field in the A/NK–A/CNK diagram (Figure 5b). The Bieruozecuo quartz diorites show a narrow range in SiO_2, from 64.07 to 68.32 wt.%, and all samples are plotted in the granodiorite field on the total alkalis-silica diagram (Figure 6a). The Th vs. Co diagram suggests that all samples are depleted in Co and Th and plot in the calc-alkaline field (Figure 6b).

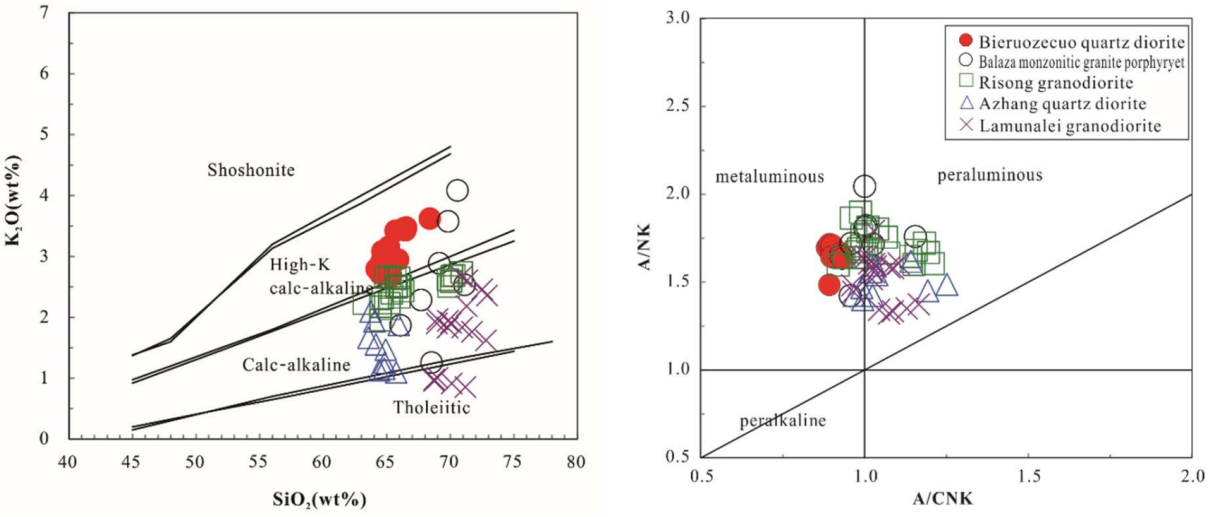

Figure 5. Diagram showing the variations in SiO_2 and K_2O concentrations of the Bieruozecuo quartz diorites and other Late Cretaceous igneous rocks within the central and northern Lhasa blocks, as well as the Miocene adakitic rocks in the southern Lhasa block. Data sources: ore-bearing porphyry in Balazha, [21]; adakitic rocks in Rutog, [24]; adakitic rocks in Azhang, [20]; adakitic rocks in Lamunale, [22].

Table 2. Major elements (wt%), trace elements (ppm) and REE (ppm) analyses of the Bieruozecuo quartz diorites.

Samples	P10(19)	P10(88)	P10(130)	P10(161)	P10(xx1)	P10(xx2)	P10(xx3)	P10(xx4)	P10(xx5)	P11(6)	P11(8)	P11(18)	P11(20)	P11(34)	P11(41)
Lithology	**Quartz Diorite**														
SiO_2	65.640	64.840	64.500	68.320	64.430	64.910	64.070	64.280	65.730	65.170	66.410	65.650	65.980	66.480	66.280
Al_2O_3	15.690	15.440	15.440	14.720	15.320	15.470	15.710	15.750	15.460	15.410	15.090	14.940	15.340	15.040	14.920
Fe_2O_3	1.790	1.860	1.890	1.260	2.110	1.980	2.050	2.100	1.820	1.410	1.140	1.380	1.170	1.830	1.290
FeO	1.940	2.280	2.080	1.590	2.330	2.300	2.270	2.150	1.950	2.970	2.890	2.830	2.610	2.330	2.800
CaO	4.130	4.340	4.210	3.620	4.320	4.120	4.660	4.660	4.060	4.460	3.890	4.150	4.030	3.900	3.790
MgO	2.140	2.530	2.400	1.600	2.670	2.440	2.540	2.430	2.140	2.060	1.840	1.990	1.760	1.830	1.830
K_2O	2.700	2.830	3.080	3.620	2.900	3.040	2.790	2.710	2.940	3.160	3.470	3.420	3.430	3.430	3.460
Na_2O	4.020	3.700	3.650	3.640	3.670	3.700	3.790	3.790	3.730	3.390	3.280	3.270	3.340	3.290	3.270
TiO_2	0.565	0.662	0.617	0.450	0.713	0.690	0.654	0.630	0.580	0.587	0.560	0.595	0.511	0.569	0.552
P_2O_5	0.189	0.235	0.228	0.160	0.253	0.239	0.264	0.266	0.238	0.115	0.112	0.129	0.102	0.115	0.123
MnO	0.064	0.063	0.069	0.058	0.073	0.066	0.067	0.062	0.059	0.075	0.073	0.072	0.073	0.073	0.078
LOI	0.767	0.787	1.440	0.653	0.777	0.603	0.697	0.747	0.832	0.712	0.765	1.040	1.220	0.713	1.160
Total	100.462	99.714	99.758	99.896	99.788	99.826	99.802	99.678	99.740	99.982	99.823	99.939	99.635	100.016	99.873
Mg#	51.792	53.286	53.087	51.151	52.953	51.588	52.390	51.744	51.533	46.418	45.581	46.558	46.136	45.064	45.163
σ	1.990	1.930	2.090	2.070	1.990	2.050	2.030	1.960	1.940	1.920	1.930	1.950	1.970	1.910	1.920
A/CNK	0.921	0.906	0.909	0.893	0.900	0.917	0.886	0.893	0.926	0.901	0.930	0.899	0.928	0.927	0.932
A/NK	1.645	1.687	1.653	1.486	1.669	1.650	1.697	1.718	1.659	1.713	1.649	1.645	1.666	1.648	1.635
$CaO + Na_2O$	8.113	8.063	7.879	7.268	8.007	7.834	8.467	8.477	7.810	7.851	7.183	7.425	7.397	7.189	7.069
Cu	9.320	22.000	27.000	6.360	18.800	44.500	19.600	25.600	29.400	33.400	29.800	22.200	24.900	29.000	29.900
Pb	9.280	18.800	14.500	13.600	22.300	29.300	22.100	19.500	22.000	13.900	15.300	15.800	7.040	14.200	20.700
Zn	53.000	67.700	61.700	46.000	71.800	71.600	71.400	61.200	63.500	69.200	53.600	49.600	49.200	50.700	69.200
Cr	44.400	63.500	50.200	32.500	59.200	50.900	57.500	56.300	48.100	32.800	20.800	27.000	23.800	22.800	23.100
Ni	22.400	35.500	28.200	20.400	32.000	29.500	30.300	28.400	25.400	13.500	10.800	12.200	10.400	11.000	11.300
Co	13.700	19.200	17.200	9.270	19.100	17.300	16.600	17.000	16.500	18.400	17.000	16.600	12.500	15.500	16.200
Rb	65.000	107.000	85.200	111.000	114.000	131.000	98.900	95.300	112.000	125.000	129.000	132.000	124.000	129.000	139.000
Cs	5.760	4.710	6.500	6.100	6.670	8.980	5.330	5.350	5.530	3.340	4.110	5.540	4.000	4.100	4.620
W	47.500	82.600	74.200	27.700	79.200	60.200	58.100	70.800	77.000	76.200	83.300	65.400	30.800	60.400	71.200
Sb	0.270	0.450	0.260	0.220	0.660	1.240	0.410	0.850	0.540	1.240	1.180	0.440	0.200	0.560	2.070
Bi	0.081	0.120	0.170	0.089	0.290	0.200	0.140	0.270	0.200	0.062	0.041	0.088	0.079	0.036	0.220
Sr	458.000	554.000	496.000	427.000	540.000	513.000	574.000	574.000	533.000	327.000	324.000	326.000	307.000	323.000	296.000
Ba	352.000	543.000	395.000	384.000	478.000	543.000	444.000	465.000	501.000	473.000	501.000	506.000	368.000	481.000	445.000
V	69.100	80.700	78.800	51.800	82.300	78.300	87.000	87.900	74.600	101.000	84.200	89.400	79.600	88.300	92.800

Table 2. *Cont.*

Samples	P10(19)	P10(88)	P10(130)	P10(161)	P10(xx1)	P10(xx2)	P10(xx3)	P10(xx4)	P10(xx5)	P11(6)	P11(8)	P11(18)	P11(20)	P11(34)	P11(41)
Lithology								**Quartz Diorite**							
Nb	9.880	10.700	9.770	9.740	11.400	11.000	11.100	10.800	11.200	10.500	10.800	11.400	8.790	11.500	13.100
Ta	0.820	0.790	0.920	0.980	0.800	0.820	0.920	0.870	0.960	0.910	0.920	0.940	0.890	1.000	1.190
Zr	98.000	44.400	92.200	118.000	65.000	49.900	65.300	75.000	69.900	98.900	92.500	104.000	87.800	155.000	94.600
Hf	3.230	1.420	3.070	3.700	1.920	1.670	2.060	2.350	2.000	3.500	2.820	3.370	3.360	5.590	3.190
Sn	1.890	2.250	2.010	1.920	2.500	2.170	3.470	2.570	2.420	1.660	1.600	2.100	1.750	1.820	2.250
Au	1.080	1.390	0.720	0.250	1.700	2.020	0.510	0.880	1.700	1.130	1.760	1.380	0.380	0.760	0.510
Ag	0.018	0.033	0.039	0.014	0.028	0.072	0.040	0.042	0.044	0.048	0.058	0.056	0.046	0.045	0.086
U	1.320	1.710	1.600	1.720	1.840	2.050	1.720	1.980	1.540	2.240	2.010	2.320	4.600	3.010	3.160
Th	7.770	9.660	11.200	12.000	15.400	11.900	9.220	12.500	12.400	11.700	12.800	13.900	16.200	20.100	17.400
Ti	0.339	0.383	0.370	0.270	0.413	0.399	0.379	0.365	0.336	0.340	0.324	0.344	0.306	0.329	0.320
La	33.200	38.400	32.200	35.600	39.000	35.800	36.100	40.400	37.000	24.800	27.600	34.200	29.900	29.600	31.200
Ce	55.400	62.300	55.200	61.000	63.500	59.800	61.300	67.200	61.800	41.900	44.800	53.400	49.000	47.100	51.000
Pr	6.460	8.370	6.580	7.250	8.120	7.670	8.170	8.670	8.040	5.350	5.730	7.000	5.650	5.990	6.700
Nd	23.500	30.600	24.300	26.200	31.200	28.900	31.900	33.400	30.100	19.700	21.400	25.200	20.100	21.900	24.400
Sm	3.870	5.140	4.110	4.360	5.240	4.990	5.500	5.620	5.060	3.660	4.080	4.780	3.590	3.940	4.610
Eu	1.100	1.300	1.070	1.080	1.290	1.300	1.350	1.410	1.280	0.980	0.950	1.070	0.940	0.920	0.950
Gd	3.230	4.340	3.300	3.550	4.340	4.200	4.600	4.720	4.150	3.380	3.660	4.310	3.170	3.450	4.040
Tb	0.430	0.560	0.440	0.460	0.560	0.520	0.620	0.610	0.530	0.490	0.550	0.620	0.470	0.500	0.570
Dy	2.230	2.650	2.380	2.320	2.740	2.710	3.080	2.940	2.660	2.960	3.230	3.580	2.700	2.850	3.340
Ho	0.420	0.490	0.430	0.440	0.520	0.480	0.570	0.540	0.480	0.580	0.620	0.700	0.560	0.570	0.650
Er	1.100	1.310	1.140	1.140	1.300	1.340	1.500	1.400	1.240	1.580	1.670	1.940	1.560	1.590	1.820
Tm	0.160	0.190	0.170	0.160	0.190	0.180	0.210	0.200	0.180	0.240	0.260	0.310	0.240	0.270	0.310
Yb	0.980	1.150	1.080	1.020	1.280	1.220	1.420	1.360	1.180	1.800	1.920	2.110	1.600	1.760	2.190
Lu	0.130	0.150	0.150	0.140	0.160	0.160	0.190	0.170	0.150	0.240	0.240	0.280	0.230	0.250	0.300
Y	9.850	11.600	10.600	10.600	12.400	11.900	13.800	12.800	11.600	14.400	15.300	17.600	14.100	14.300	16.500
La/Yb	33.878	33.391	29.815	34.902	30.469	29.344	25.423	29.706	31.356	13.778	14.375	16.209	18.688	16.818	14.247
Sr / Y	46.497	47.759	46.792	40.283	43.548	43.109	41.594	44.844	45.948	22.708	21.176	18.523	21.773	22.587	17.939
∑REE	132.210	156.950	132.550	144.720	159.440	149.270	156.510	168.640	153.850	107.660	116.710	139.500	119.710	120.690	132.080
δEu	0.934	0.827	0.868	0.821	0.811	0.853	0.806	0.822	0.836	0.845	0.744	0.713	0.841	0.753	0.664
$(La/Yb)_N$	22.316	21.996	19.640	22.991	20.071	19.330	16.747	19.568	20.655	9.076	9.469	10.677	12.310	11.079	9.385

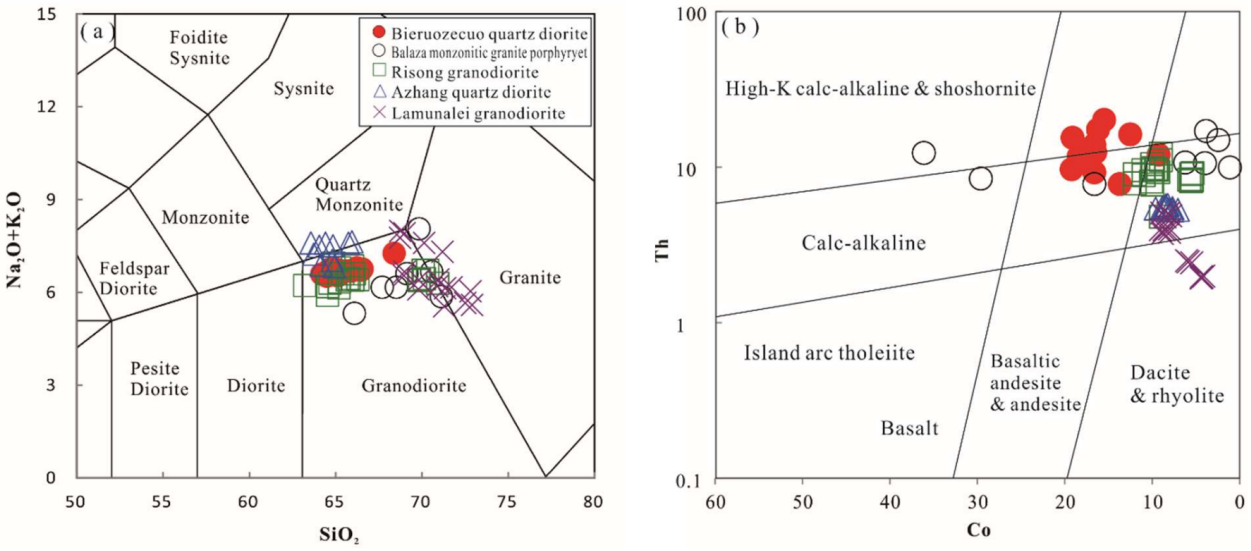

Figure 6. (**a**) TAS classification and nomenclature diagram [25]; (**b**) Th–Co diagram showing sample compositional variations, after [26].

The trace and REE composition of the Bieruozecuo quartz diorites are consistent with previously reported Cretaceous adakitic rocks in the Lhasa block (Figure 7), suggesting a possible genetic relationship. All the rocks are characterized by the enrichment of light rare earth elements (LREEs) and depletion of heavy rare earth elements (HREEs) [$(La/Yb)_N$ =9.08–22.99, Figure 7a]. The REE contents of the quartz monzonite are much lower than the mean value of the upper crust (210.10 ppm) [27] and display slightly negative Eu anomalies (Eu/Eu* = 0.66–0.94). All rocks exhibit overall enriched large ion lithophile elements (LILE, e.g., Rb and K) and LREE, and are depleted in high field strength elements (HFSE, e.g., Nb, Ti, and P; Figure 7b). The samples show marked Nb and Ti negative anomalies. Nb negative anomaly is a feature of the continental crust [28], indicating crustal materials are involved in the magmatic source [29] of the Bieruozecuo quartz diorites. These plutonic rocks also show high Sr content (296.00–574.00 ppm), high Sr/Y ratio (17.94–47.76), low Y content (9.85–17.60 ppm) and Yb content (0.98–2.19 ppm), which are comparable with adakitic composition (Figure 8).

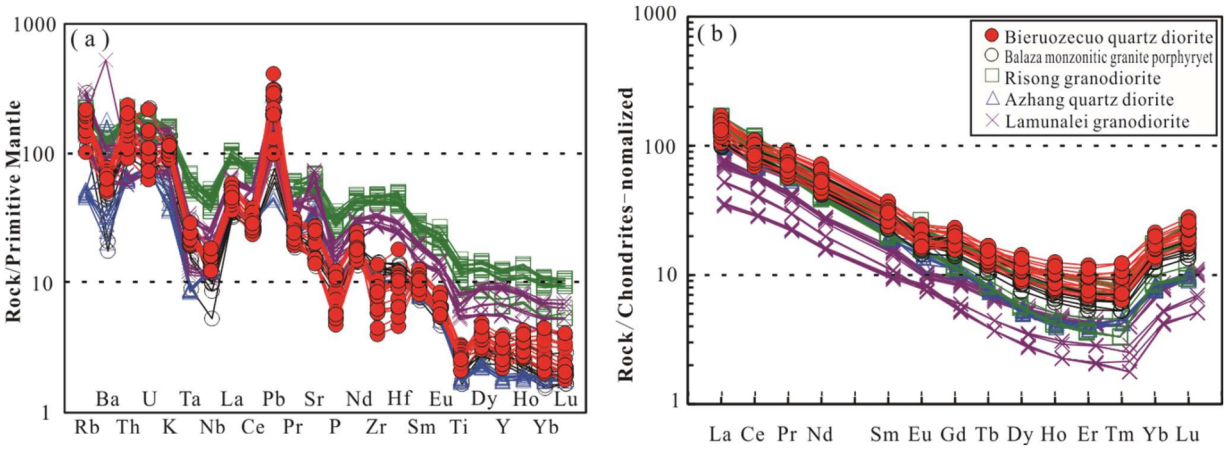

Figure 7. (**a**) Primitive mantle-normalized trace element spider diagrams (normalization values, after [30]); (**b**) chondrite-normalized REE patterns (normalization values, after [31]).

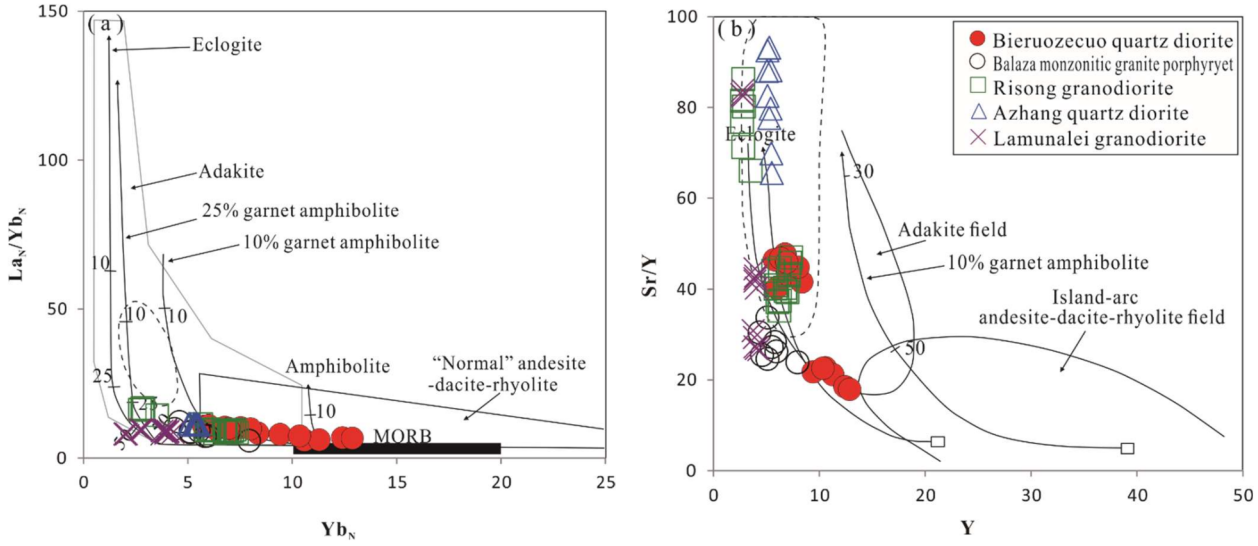

Figure 8. (**a**) (La/Yb) N vs. YbN [32,33] and (**b**) plots of Sr/Y vs. Y [34].

5. Discussion

5.1. Geochemical Classification

The "adakite" was first proposed by [34], which is considered to be one type of intermediate-felsic igneous rock with special geochemical characteristics. These adakite rocks usually have the following characteristic: SiO_2 > 56 wt.%, Al_2O_3 > 15 wt.%, MgO < 3 wt.%, Sr/Y ratio (>20, depleted in Y (<18 ppm) and HREE (Yb < 19 ppm), high Sr (>400 ppm or 300 ppm) (positive or without Eu), and Sr anomalies (depleted in high field strength elements) [33,35–38]. The generation of adakites was initially proposed to be related to the partial melting of the young and hot subducted oceanic lithosphere under eclogite facies condition [34,38], although their origin is much more complex. Many studies show that some igneous rocks with adakite-like geochemical affinities are actually unrelated to slab melting, and they proposed a broad definition of adakites, compassing a wide range of island arc magmatic rocks and collision-related rocks [36,39]. Thus, the term "adakitic" is proposed to distinguish rocks with adakite-like geochemical features to those rocks formed by slab melting [39–41]. At present, many rocks are classified as adakitic, and many studies show that adakitic rocks and typical adakites can be formed in several geodynamic settings, including oceanic subduction, syn-collision, post-collision extension, and within-plate rifting [35–41]; thus, adakitic rocks and typical adakites are one key probe to study the tectonic evolution of paleo-orogenic belt.

The studied Bieruozecuo quartz diorites samples have high contents of SiO_2 (64.07–68.32 wt.%) and Al_2O_3 (14.72–15.75 wt.%), with high Sr/Y (21.18–47.76) and La/Yb (13.78–34.90), as well as low MgO (1.60–2.67 wt.%), Y (9.850–16.500 ppm), and Yb (0.980–2.190 ppm). The geochemical discrimination diagrams of $(La/Yb)_N$ vs. Yb_N and Sr/Y vs. Y show that the studied Bieruozecuo quartz diorites exhibits typical adakitic geochemical affinities (Figure 8). Previous studies have reported several ca. 90~82 Ma adakitic plutons in the north and central Lhasa blocks. The Bieruozecuo quartz diorites studied in this paper has similar geochemical composition and crystallization age to those reported adakitic plutons (Figures 5–8), suggesting that the adakitic magmatic activity in the north and central Lhasa blocks may last from 116 Ma to 82 Ma.

5.2. Petrogenesis

Numerous studies show that the petrogenesis of intermediate igneous rocks is complex and various, including the mixing of mantle-derived mafic magma and granitic magma, partial melting of mafic crust, and AFC of mantle-derived magma [42–44]. The Early Cretaceous Bieruzecuo quartz diorites are meta-aluminous high-K calc-alkaline plutonic rock, with high K_2O (average content of 3.13 wt.%) and low CaO (average content of

4.16 wt.%), indicating that the magma mainly originated from the partial melting of continental crust [45]. The trace elements of Cr (20.8–63.5 ppm, with an average of 40.9 ppm), Ni (10.4–32.0 ppm, with an average of 21.4 ppm), and Co (9.3–19.2 ppm, with an average of 16.1 ppm) are very close to the continental crust, and the La/Nb ratios (2.38–3.74) are significantly different from mantle-derived magma (La/Nb ≈ 0.96) [30]. Nb and Ta are stable in the process of erosion and metamorphism and have the characteristics of tracing magma origin [46,47]. The Nb/Ta ratios of the Late Early Cretaceous quartz diorite is 9.88–13.54, which is close to the average crustal value (12–13) but significantly lower than the mantle magma value (17 ± 1, [48]). The Nd/Th ratios (1.09–3.46) are consistent with the Nd/Th ratio for the crustal source (≈3) and significantly lower than that of the mantle source (>15) [49], suggesting that the magma may not derive from partial melting of mantle peridotite or separation and crystallization of basaltic magma [50], but from partial melting of continental crustal rocks [51]. The Ti/Zr ratios (21.23–86.26, average 44.97) and Ti/Y ratios (193.94–349.06, average 272.02) are slightly higher than those of continental crust rocks (Ti/Zr < 30, Ti/Y < 200) [52], which may be related to the presence of garnet residues in the source [53] and resemblance with the high La/Yb and Sr/Y ratios of rocks.

The Bieruzecuo quartz diorites have the geochemical characteristics of adakitic rocks. According to previous works, the genesis of adakitic rocks may be due to: (1) partial melting of young oceanic crust [34,40,54–56]; (2) fractional crystallization of primitive basaltic magma and assimilation with crustal materials, i.e., the AFC model [34,57]; (3) magma mixing between felsic and mafic magmas [58,59]; (4) partial melting of a thickened lower crust or delaminated lower crust under high-temperature conditions [38,60,61]; and (5) partial melting of subducted continental crust [38,61]. The Bieruzecuo adakitic rocks have high SiO_2 content (65–69.32 wt.%); there is no obvious Eu anomaly in the REE patterns, and the rocks do not show assemblages of gabbro–diorite–granodiorite, which precludes the AFC model of the geochemical trends in Rb/Nd vs. Rb, and the La/Sm vs. Sm diagrams do not support the AFC model (Figure 9). As mentioned above, the Bieruzecuo quartz diorites are mainly derived from the partial melting of continental crust materials, which is consistent with their high ratios of K_2O/Na_2O (Figure 10A).

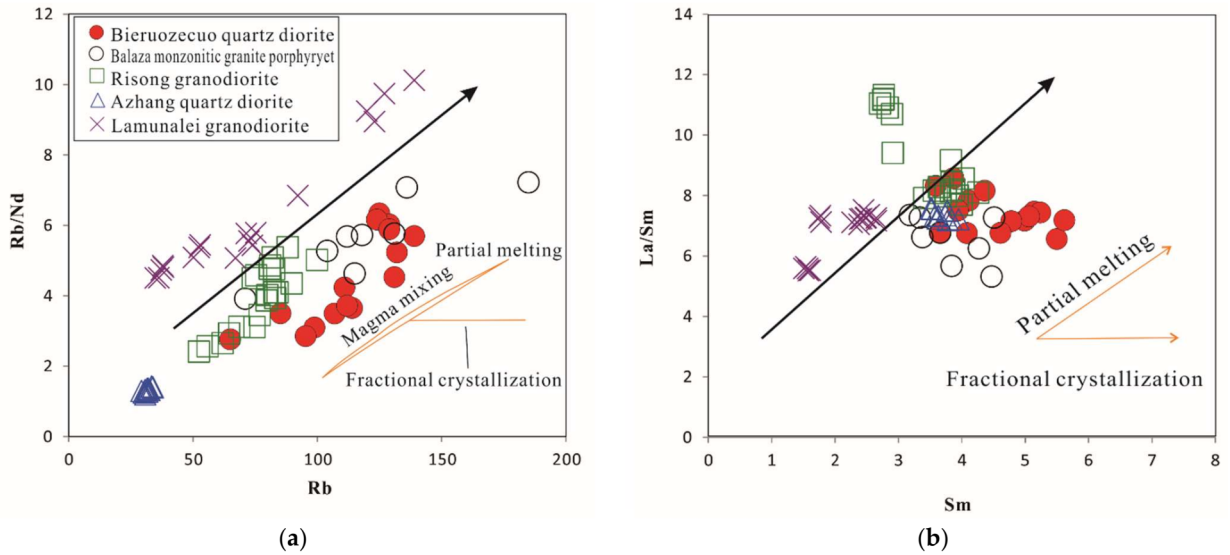

Figure 9. Discrimination diagrams of petrogenetic processes of the Bieruozecuo quartz diorites. (**a**) Rb/Nd s. Rb (after [62]); (**b**) La/Sm s. La (after [63]).

Based on the geochemical characteristics of the Bieruozecuo adakites, we propose that the studied adakites may be the product of partial melting of the delaminated lower crust. In general, the adakite formed by partial melting of the delaminated lower crust is easy to modify via the addition of mantle materials during magma ascending and emplacement, resulting in high MgO, Cr, and Ni contents in the rocks [21,40,64,65]. The studied adakites

have high Mg#, Cr (20.80–63.50 ppm), and Ni (10.40–32.00 ppm), resembling the rocks that derived from the melting of the delaminated lower crust or subducted oceanic crust, but differ from the adakite formed by partial melting of the thickened lower crust (Figure 10). However, the geochemical features of the high ratios of K_2O/Na_2O and low ratios of CaO/Al_2O_3 strongly exclude the model of the melting of the subducted oceanic crust (Figure 10a). Thus, the melting of the delaminated continental lower crust is proposed to be the most possible model for the origin of the studied adakitic rocks in the northern Lhasa block.

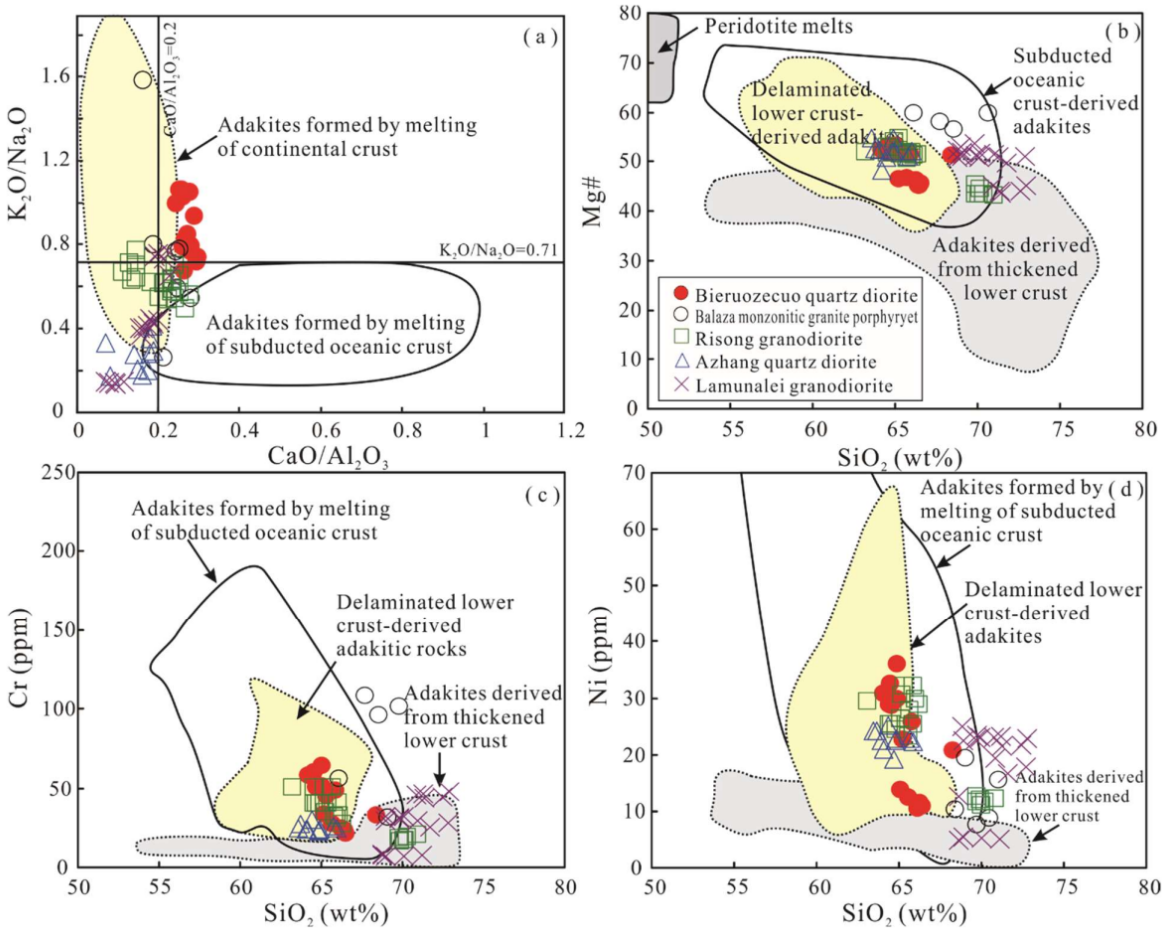

Figure 10. Relationship diagram of geochemical characteristics of the major elements for the Bieruozecuo adakitic rocks. Diagram (**a**) after [66]; (**b**) after [67]; (**c**) after [68]; (**d**) after [68].

5.3. Tectonic Setting and Geological Significance

Previous studies show that the Tethyan ophiolites, along the BNSZ, are overlain unconformably by clastic sequences of the Lower Cretaceous Dongqiao Formation (ca. 130−118 Ma) [7,9,14]. This relationship suggests that the BNSZ ocean basin was closed in the Early Cretaceous, and collision between north Lhasa and Qiangtang blocks occurred at the Early Cretaceous [69]. However, the transition from syn-collision to post-collisional extension is still unclear, resulting in the discussion of the geodynamic setting of the Cretaceous magmatism in the Lhasa block.

As shown in Figure 1, the Early Cretaceous is an important magmatic activity period in the Lhasa block, which occurs almost simultaneously in the south (ca. 100–137 Ma), the central (ca. 95–145 Ma), and north Lhasa blocks (ca. 110–133 Ma). The peak period of magmatic activity is concentrated in ca. 120–110 Ma [2,70], and the Bieruozecuo adakitic quartz diorite is the product of this peak magmatism. Recent studies have shown that the collision between the Lhasa and Qiangtang blocks in Early Cretaceous may result in the thickening of the continental crust of the north Lhasa block [7,69]. As shown in Figure 11,

The Bieruzecuo quartz diorites mostly fall in the field of volcanic arc granites (VAG). The ca. 116–114 Ma Bieruozecuo quartz diorite has the geochemical characteristics identical to magmas originating from delaminated crust, which indicates, once again, that the large-scale adakitic magmatism in the northern and central Lhasa blocks is the response to the delamination of continental lower crust, as well as the tectonic transition from syn-collision to post-collisional extension, occurring at ca. 120–110 Ma.

Therefore, we propose that the Bieruzecuo pluton is the product of post-collisional extension and derived from the partial melting of the delaminated continental lower crust. Continental crust delamination may be responsible for the post-collisional extension, which is an important mechanism to the ca. 120–110 Ma adakitic magmatism flare-up event in the Lhasa block (Figure 12).

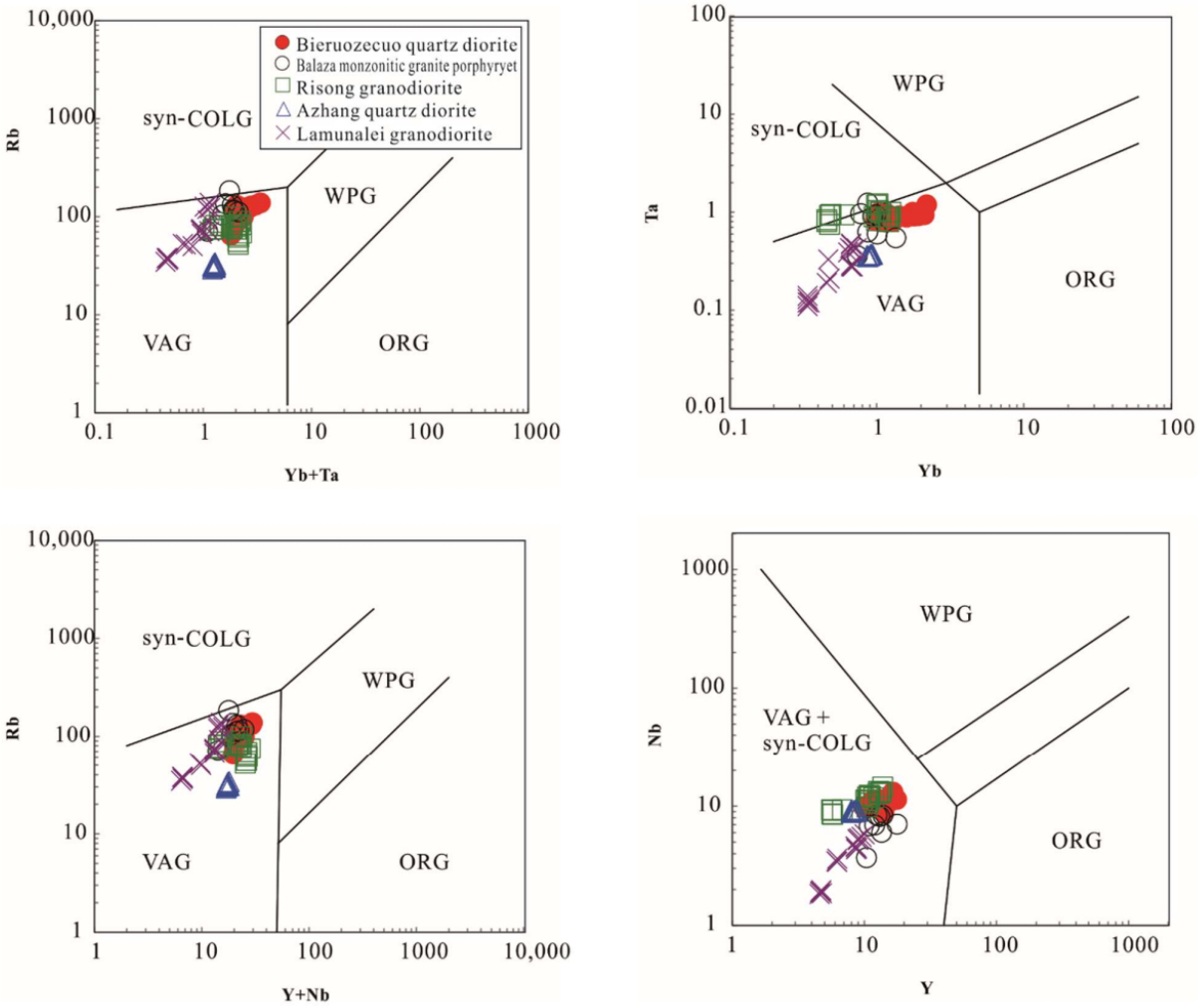

Figure 11. Bulk geochemical data for the Bieruozecuo adakitic rock from the Lhasa block, Tibet, plotted on the Pearce diagram [71].

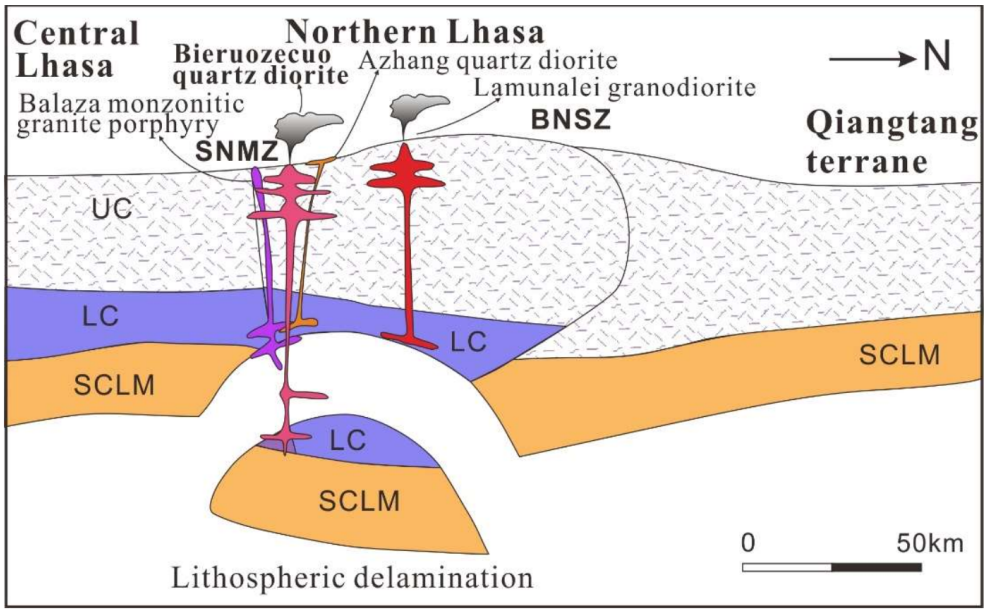

Figure 12. Schematic illustration showing the geodynamic evolution of the central–northern Lhasa subterrane, at ca. 120–110 Ma. BNSZ = Bangong–Nujiang suture zone; SNMZ = Shiquan River–Nam Tso mélange zone; UC= upper crust; LC = lower crust; and SCLM = sub-continental lithospheric mantle.

6. Conclusions

(1) LA–ICP–MS zircon U–Pb geochronology shows that the Bieruozecuo quartz diorite from north Lhasa block crystallized at ca. 116–114 Ma (Early Cretaceous magmatic event).

(2) The Bieruozecuo quartz diorite was enriched in Al_2O_3 and Na_2O, but relatively depleted in TiO_2, MgO, and MnO, which may be included in the quasi-alumina high-K calc-alkaline series. They display the geochemical characteristics typical of adakitic rocks, with high Sr, low Y and Yb, as well as high Sr/Y and La/Yb ratios. The high Mg#, K_2O/Na_2O ratios, Cr, and Ni contents indicate that these adaktic rocks probably derived from the partial melting of the delaminated continental crust, without obvious fractional crystallization during magma ascending and emplacement.

(3) The Early Cretaceous flare-up event of adaktic magmatism of the Lhasa block is a response to the delamination of continental crust, as well as the transition from syn-collision to post-collisional extension at ca. 120–110 Ma.

Author Contributions: Conceptualization, Q.-R.X. and Y.-F.W.; methodology, F.-H.X.; software, Z.-Y.L.; formal analysis, Q.-R.X., Y.-F.W., and Z.-Y.L.; investigation, Y.-F.W. and Z.-Y.L.; resources, Y.-F.W.; data curation, Q.-R.X. and J.-X.W.; writing—original draft preparation, Q.-R.X.; writing—review and editing, F.-H.X. and L.F.; visualization, Q.-R.X., L.F., and H.Z.; project administration, Y.-F.W.; funding acquisition, Y.-F.W. All authors have read and agreed to the published version of the manuscript.

Funding: This work was supported by the project, named Geological and Mineral Survey, of Gzezao Bieruozuo, 1:50,000, in Tibet (I44E022020, I44E022021, I44E023020, I44E023021).

Data Availability Statement: The data supporting reported results can be found in the text.

Acknowledgments: We gratefully acknowledge the research members, who are Zeng Wei, Shao Zhiwei, Yu Xuhui, Tang Guangcheng, Zhu Guobao, etc., for their cooperation and help.

Conflicts of Interest: The authors declare no conflict of interest.

References

1. Mo, X.X.; Dong, G.C.; Zhao, Z.D.; Zhou, S.; Wang, L.L.; Qiu, R.Z.; Zhang, F.Q. Spatial and Temporal Distribution and Characteristics of Granitoids in the Gangdese, Tibet and Implication for Crustal Growth and Evolution. *Geol. J. China Univ.* **2005**, *11*, 281–290.
2. Zhu, D.C.; Pan, G.T.; Mo, X.X.; Wang, L.Q.; Liao, Z.L.; Zhao, Z.D.; Dong, G.C.; Zhou, C.Y. Late Jurassic-Early Cretaceous geodynamic setting in middle-northern Gandese: New insights from volcanic rocks. *Acta Petrol. Sin.* **2006**, *22*, 534–546.
3. Zhu, D.C.; Pan, G.T.; Wang, L.Q.; Mo, X.X.; Zhao, Z.D.; Zhou, C.Y.; Liao, Z.L.; Dong, G.C.; Yuan, S.H. Spatial-temporal distribution and tectonic setting of Jurassic magmatism in the Gangdise belt, Tibet, China. *Geol. Bull. China* **2008**, *4*, 458–468.
4. Ma, G.L.; Yue, Y.H. Cretaceous volcanic rocks in northern Lhasa block: Constraints on the tectonic evolution of the Gangdese arc. *Acta Petrol. Mineral.* **2010**, *29*, 525–538. (In Chinese)
5. Wu, Z.H.; Wu, X.W.; Zhao, Z.; Lu, L.; Ye, P.S.; Zhang, Y.L. Shrimp U-Pb isotopic dating of the Late Cretaceous volcanic rocks and its chronological constraint on the red-beds in southern Qiangtang Block. *Acta Geosci. Sin.* **2014**, *35*, 567–572. (In Chinese)
6. Zhang, S.; Shi, H.F.; Hao, H.J.; Li, D.W.; Lin, Y.; Feng, M.X. Geochronology, geochemistry and tectonic significance of Late Cretaceous adakites in Bangong Lake, Tibet. *Earth Sci. (J. China Univ. Geosci.)* **2014**, *39*, 509–524, (In Chinese with English abstract).
7. Kapp, P.; DeCelles, P.G.; Gehrels, G.E.; Heizier, M.; Ding, L. Geological records of the Lhasa-Qiangtang and Indo-Asian collisions in the Nima area of central Tibet. *Geol. Soc. Am. Bull.* **2007**, *119*, 917–933. [CrossRef]
8. Wen, D.R.; Liu, D.Y.; Chung, S.L.; Chu, M.F.; Ji, J.Q.; Zhang, Q.; Song, B.; Lee, T.Y.; Yeh, M.W.; Lo, C.H. Zircon SHRIMP U-Pb ages of the Gangdese Batholith and implications for Neotethyan subduction in southern Tibet. *Chem. Geol.* **2008**, *252*, 191–201. [CrossRef]
9. Zhu, D.C.; Mo, X.X.; Niu, Y.L.; Zhao, Z.D.; Wang, L.Q.; Liu, Y.S.; Wu, F.Y. Geochemical investigation of Early Cretaceous igneous rocks along an east−west traverse throughout the central Lhasa Terrane, Tibet. *Chem. Geol.* **2009**, *268*, 298–312. [CrossRef]
10. Zhu, D.C.; Zhao, Z.D.; Niu, Y.L.; Mo, X.X.; Chung, S.L.; Hou, Z.Q.; Wu, F.Y. The Lhasa Terrane: Record of a microcontinent and its histories of drift and growth. *Earth Planet. Sci. Lett.* **2011**, *301*, 241–255. [CrossRef]
11. Powell, C.M.; Conaghan, P.J. Plate tectonics and the Himalayas. *Earth Planetaru Sci. Lett.* **1973**, *20*, 1–12. [CrossRef]
12. Molnar, P.; Tapponnier, P. Cenozoic tectonice of Asia: Effects of a continental collision: Features of recent continental tectonics in Asia can be interpreted as results of the India-Eurasia collision. *Science* **1975**, *189*, 419–426. [CrossRef] [PubMed]
13. Pan, G.T.; Chen, Z.L.; Li, X.Z.; Yan, Y.J.; Xu, X.S.; Xu, Q.; Jiang, X.S.; Wu, Y.L.; Luo, J.N.; Zhu, T.X.; et al. *Geological-Tectonic Evolution in the Eastern Tethys*; Grological Publishing House: Beijing, China, 1997; pp. 1–218. (In Chinese)
14. Yin, A.; Harrison, T.M. Geologic evolution of the Himalayan-Tibetan Orogen. *Annu. Rev. Earth Planet. Sci.* **2000**, *28*, 211–280. [CrossRef]
15. Xu, Z.Q.; Yang, J.S.; Li, W.C.; Li, H.Q.; Cai, Z.H.; Yan, Z.; Ma, C.Q. Paleo- Tethys system and accretionary orogeny in the Tibet Plateau. *Acta Petrol. Sin.* **2013**, *29*, 1847–1860, (In Chinese with English abstract).
16. Mo, X.X.; Niu, Y.L.; Dong, G.C.; Zhao, Z.D.; Hou, Z.Q.; Zhou, S.; Ke, S. Contribution of syncollisional felsic magmatism to continental crus growth: A case study of the Paleogene Linzizong volcanic succession in southern Tibet. *Chem. Geol.* **2008**, *250*, 49–67. [CrossRef]
17. Wang, Z.Z.; Liu, D.; Zhao, Z.D.; Yan, J.J.; Shi, Q.S.; Mo, X.X. The Sangri highly fractionated I-type granites in southern Gangdese: Petrogenesis and dynamic implication. *Acta Petrol. Sin.* **2017**, *22*, 2479–2493. (In Chinese)
18. Wu, F.Y.; Ji, W.Q.; Liu, C.Z.; Chung, S.L. Detrital zircon UePb and Hf isotopicdata from the Xigaze fore-arc basin: Constraints on Transhimalayan. *Chem. Geol.* **2010**, *271*, 13–25. [CrossRef]
19. Huang, S.H.; Chen, J.L.; Zen, Y.C.; Tan, R.Y.; Huang, T.T.; Liu, X.J. Geochemical characteristics of Early Cretaceous magmatic rocks in the northwestern part of the Lhasa Block and indications of early crustal growth of the southern plateau. *Geochimica* **2020**, *49*, 21–35.
20. Sun, G.Y.; Hu, X.M.; Zhu, D.C.; Hong, W.T.; Wang, J.G.; Wang, Q. Thickened juvenile lower crust-derived ~90 Ma adakitic rocks in the central Lhasa terrane, Tibet. *Lithos* **2015**, *224*, 225–239. [CrossRef]
21. Yu, H.X.; Chen, J.L.; Xu, J.F.; Wang, B.D.; Wu, J.B.; Liang, H.Y. Geochemistry and origin of Late Cretaceous(~90 Ma) ore-bearing porphyry of Balazha in mid-northern Lhasa terrane, Tibet. *Acta Petrol. Sin.* **2011**, *27*, 2011–2022, (In Chinese with English abstract).
22. Dong, Y.C.; Wang, M.; Xie, C.M.; Yu, Y.P.; Hao, Y.J. Genesis and tectonic indication of the Late Cretaceous adakite rocks in the Lamunale area, Nima County, Tibet. *Acta Petrol. Sin.* **2020**, *36*, 426–442.
23. Hou, K.J.; Li, Y.H.; Tian, Y.R. In situ U-Pb zircon dating using laser ablation-multi ion counting-ICP-MS. *Miner. Depos.* **2009**, *28*, 481–492.
24. Zhang, X.F.; Li, Y.G.; Cao, X.M.; Qu, X.M.; Xin, H.B.; Wang, J.; Du, D.D. LA-ICP-MS zircon U-Pb age and geochemical characteristics of the acid intrusive rocks in the western part of Bangong Lake-Nujiang River suture zone. *Geol. Bull. CHN.* **2014**, *33*, 984–994, (In Chinese with English abstract).
25. Middlemost, E.A.K. Naming materials in the magma/igneous rock system. *Earth-Sci. Rev.* **1994**, *37*, 215–224. [CrossRef]
26. Hastie, A.R.; Kerr, A.C.; Pearce, J.A.; Mitchell, S.F. Classification of altered volcanic island arc rocks using immobile trace elements: Development of the Th-Co discrimination diagram. *J. Petrol.* **2007**, *48*, 2341–2357. [CrossRef]
27. Maniar, P.D.; Piccoli, P.M. Tectonic discrimination of granitoids. *Geol. Soc. Am. Bull.* **1989**, *101*, 635–643. [CrossRef]
28. Jiang, Y.H.; Yang, W.Z. Geochemistry of early Yanshanian granitoids and its tectonic significance in the western Qinghai-Tibet plateau. *Mineral. Petrol.* **2000**, *20*, 74–79.

29. Zhong, H.M.; Tong, J.S.; Lu, R.K.; Xia, J. Geochemical characteristics and tectonic setting of peraluminous granite in the Songxi area, Rutog County, Tibet, China. *Geol. Bull. China* **2006**, *25*, 183–188.
30. Sun, S.S.; McDonough, W.F. Chemical and isotopic systematics of oceanic basalts: Implications for mantle composition and processes. In *Magmatism in Occean Basins*; Sander, A.D., Norry, M.H., Eds.; Geological Society of London Special Publications: London, UK, 1989; Volume 42, pp. 313–345.
31. Taylor, S.R.; McLennan, S.M. *The Continental Crust: Its Composition and Evolution*; U.S. Department of Energy: Washington, DC, USA, 1985.
32. Drummond, M.S.; Defant, M.J. A model for trondhjemite–tonalite–dacite genesis and crustal growth via slab melting: Archaean to modern comparisons. *J. Geophys. Res.* **1990**, *95*, 21503–21521. [CrossRef]
33. Martin, H. Adakitic magmas: Modern analogues of Archaean granitoids. *Lithos* **1999**, *46*, 411–429. [CrossRef]
34. Defant, M.J.; Drummond, M.S. Derivation of some modern are magmas by melting of young subducted lithosphere. *Nature* **1990**, *327*, 662–665. [CrossRef]
35. Clemens, J. D S-type granitic magmas: Petrgenetic issues, models and evidene. *Earth-Sci. Rev.* **2003**, *61*, 1–18. [CrossRef]
36. Castillo, P.R. An overview of adakite petrogenesis. *Chin. Sci. Bull.* **2006**, *51*, 257–268. [CrossRef]
37. Castillo, P.R. Adakite petrogenesis. *Lithos* **2012**, *134,135*, 304–316. [CrossRef]
38. Wang, Q.; Xu, J.F.; Zhao, Z.H.; Zi, F.; Tang, G.J.; Jia, X.H.; Jiang, Z.Q. Tectonic setting and associated rock suites of adakitc rocks. *Bull. Mineral. Petrol. Geochem.* **2008**, *27*, 344–350. (In Chinese)
39. Moyen, J.F. High Sr/Y and La/Yb ratios: The meaning of the "adakitic signature". *Lithos* **2009**, *112*, 556–574. [CrossRef]
40. Martin, H.; Smithies, R.H.; Rapp, R.; Moyen, J.F.; Champion, D. An overview of adakite, tonalite-trondhjemite-granodiorite(TTG), and sanukitoid: Relationships and some implications for crustal evolution. *Lithos* **2005**, *79*, 1–24. [CrossRef]
41. Xu, J.F.; Wu, J.B.; Wang, Q.; Chen, J.L.; Cao, K. Research advances of adakites and adakitic rocks in China. *Bull. Mineral. Petrol. Geochem.* **2014**, *33*, 6–13, (In Chinese with English abstract).
42. Arnaud, N.O.; Vidal, P.H.; Tapponnier, P.; Matte, P.H.; Deng, W.M. The high K_2O volcanism of northwestern Tibet: Geochemistry and tectonic implications. *Earth Planet. Sci. Lett.* **1992**, *111*, 351–367. [CrossRef]
43. Thompson, A.B. Fertility of crusta1 rocks during anatexis. *Trans. R. Soc. Edinburgh Earth Sci.* **1996**, *87*, 1–10.
44. Wang, Y.J.; Fan, W.M.; Guo, F. Geochemistry of early Mesozoic potassium-rich diorites-granodiorites in southeastern Hunan Province, South China: Petrogenesis and tectonic implications. *Geochem. J.* **2003**, *37*, 427–448. [CrossRef]
45. Xiao, Q.H.; Deng, J.F.; Ma, D.Q.; Hong, D.W.; Mo, X.X.; Lu, X.X.; Li, Z.C.; Wang, X.W.; Ma, C.Q.; Wu, F.Y.; et al. *Thinking and Method of Granite Research*; Geological Publishing House: Beijing, China, 2002; pp. 12–20.
46. Barth, M.G.; McDonough, W.; Rudnick, R. Tracking the budget of Nb and Ta in the continental crust. *Chem. Geol.* **2000**, *165*, 197–213. [CrossRef]
47. Pfänder, J.A.; Münker, C.; Stracke, A.; Mezger, K. Nb/Ta and Zr/Hf in ocean island basalts - implications for crust-mantle differentiation and the fate of Niobium. *Earth Planet. Sci. Lett.* **2007**, *254*, 158–172. [CrossRef]
48. Green, T.H. Significance of Nb/Ta as an indicator of geochemical processes in the crust-mantle system. *Chem. Geol.* **1995**, *120*, 347–359. [CrossRef]
49. Bea, F.; Arzamastsev, A.; Montero, P.; Arzamastseva, L. Aonmalous alkaline rocks of Soustov, Kola:evidence of mantle-derived matasomatic fluids affecting crustal materials. *Contrib. Min. Pet.* **2001**, *140*, 554–566. [CrossRef]
50. Li, S.G.; Nie, Y.H.; Zhen, S.G. Interaction between subducted continental crust and upper mantle—I. Geochemistry of major elements and trace elements in the synchromatic mafic-ultramafic rocks in Dabieshan. *China Sci.* **1997**, *27*, 488–493.
51. Xie, L.; Dun, D.; Zhu, L.D.; Ni, M.C.; Yang, W.G.; Tao, G.; Li, C.; He, B.; He, Y. Zircon U-Pb geochronology, geochemistry and geological significance of the Zhaduding A-type granites in northern Gangdise, Tibet. *Geol. China* **2015**, *42*, 1214–1227.
52. Wedepohl, K.H. The composition of the continental crust. *Geochim. Cosmochim. Acta* **1995**, *59*, 1217–1232. [CrossRef]
53. Zhang, Z.Z.; Gu, L.X.; Wu, C.Z.; Zhai, J.P.; Wang, C.S.; Tang, J.H.; Xiao, E. Early-Middle Indosinian Weiya Quartz Diorite, Eastern Segment of the Middle Tianshan Mountains, NW China: Implications for Intra-Continent Subduction and Partial Melting of Juvenile Lower Crust. *Acta Geol. Sin.* **2011**, *85*, 1420–1434.
54. Rapp, R.P.; Shimizu, N.; Norman, M.D.; Applegate, G.S. Reaction between slab-derived melts and peridotite in the mantle wedge: Experimental constraints at 3.8GPa. *Chem. Geol.* **1999**, *160*, 335–356. [CrossRef]
55. Zhang, Z.M.; Zhao, G.C.; Santosh, M.; Wang, J.L.; Dong, X.; Shen, K. Late Cretaceous charnockite with adakitic affinities from the Gangdese batholith, shoutheastern Tibet: Evidence for Neo-Tethyan mid-ocean ridge subdution? *Gondwana Res.* **2010**, *17*, 615–631. [CrossRef]
56. Eyuboglu, Y.; Chung, S.L.; Santosh, M.; Dudas, F.O.; Akaryali, E. Transition from shoshonitic to adakitic magmatism in the eastern Pontides, NE Turkey: Implications for slab window melting. *Gondwana Res.* **2011**, *19*, 413–429. [CrossRef]
57. Kang, Z.Q.; Xu, J.F.; Wang, B.D.; Dong, Y.H.; Wang, S.Q.; Chen, J.L. Geochemistry of Cretaceous volcanic rocks of Duoni Formation in northern Lhasa Block: Discussion of tectonic setting. *Earth Sci. (J. China Univ. Geosci.)* **2009**, *34*, 89–104. (In Chinese)
58. Guo, F.; Nakamuru, E.; Fan, W.; Kobayoshi, K.; Li, C. Generation of Palaeocene adakitic andesites by magma mixing in Yanji Area, NE China. *J. Petrol.* **2007**, *48*, 661–692. [CrossRef]
59. Streck, M.J.; Leeman, W.P.; Chesley, J. High-magnesian andesite from Mount Shasta: A product of magma mixing and contamination, not a primitive mantle melt. *Geology* **2007**, *35*, 351–354. [CrossRef]

60. Wang, Q.; McDermott, F.; Xu, J.F.; Bellon, H.; Zhu, Y.T. Cenozoic K-rich adakitic volcanic rocks in the Hohxil area, northern Tibet: Lower-crustal melting in an intracontinental setting. *Geology* **2005**, *33*, 465–468. [CrossRef]
61. Lai, S.C.; Qin, J.F. Adakitic rocks derived from the partial melting of subducted continental crust: Evidence from the Eocene volcanic rocks in the northern Qiangtang block. *Gondwana Res.* **2013**, *23*, 812–824. [CrossRef]
62. Schiano, P.; Monzier, M.; Eissen, J.P.; Martin, H.; Koga, K.T. Simple mixing as the major control of the evolution of volcanic suites in the Ecuadorian Andes. *Contrib. Mineral. Petrol.* **2010**, *160*, 297–312. [CrossRef]
63. Wu, H.; Li, C.; Xu, M.J.; Li, X.K. Early cretaceous adakitic magmatism in the Dachagou Area, northern Ihasa terrane, Tibet: Implications for slab roll-back and subsequent slab break-off of the lithosphere of the Bangong-Nujiang Occan. *J. Asian Earth Sci.* **2015**, *97*, 51–66. [CrossRef]
64. Smithies, R.H. The Archaean tonalite-tonalite-trondhjemite-granodiorite (TTG) series is ont an analogue of Cenozoic adakite. *Earth Planetaru Sci. Lett.* **2000**, *182*, 115–125. [CrossRef]
65. Prouteau, G.; Scaillet, B.; Pichabant, M.; Maury, R. Evidence for mantle metasomatism by hydrous silicic melts derived from subducted oceanic crust. *Nature* **2001**, *410*, 197–200. [CrossRef] [PubMed]
66. Chen, J.; Wei, J.; Fu, L.; Li, H.; Zhou, H.; Zhao, X.; Zhan, X.; Tan, J. Multiple sources of the Early Mesozoic Gouli batholith, Eastern Kunlun Orogenic Belt, northern Tibetan Plateau: Linking continental crustal growth with oceanic subduction. *Lithos* **2017**, *292–293*, 161–178. [CrossRef]
67. Wang, Q.; Wyman, D.A.; Xu, J.F.; Zhao, Z.H.; Jian, P.; Xiong, X.L.; Bao, Z.W.; Li, C.F.; Bai, Z.H. Petrogenesis of Cretaceous adakitic and shoshonitic igneous rocks in the Luzong area, Anhui Province (eastern China): Implications for geodynamics and Cu-Au mineralization. *Lithos* **2006**, *89*, 424–446. [CrossRef]
68. Huang, X.L.; Xu, Y.G.; Lan, J.B.; Yang, Q.J.; Luo, Z.Y. Neoproterozoic adakitic rocks from Mopanshan in the western Yangtze Craton: Partial melts of a thickened lower cnust. *Lithos* **2009**, *1*, 367–381. [CrossRef]
69. Zhu, D.C.; Li, S.M.; Cawood, P.A.; Wang, Q.; Zhao, Z.D.; Liu, S.A.; Wang, L.Q. Assembly of the Lhasa and QIangtang terranes in central Tibet by divergent double subduction. *Lithos* **2016**, *245*, 7–17. [CrossRef]
70. Zhu, D.C.; Pan, G.T.; Wang, L.Q.; Mo, X.X.; Zhao, Z.D.; Zhou, C.Y.; Liao, Z.L.; Dong, G.C.; Yuan, S.H. Tempo-spatial variations of Mesozoic magmatic rocks in the Gangdise belt, Tibet, China, with a discussion of geodynamic setting-related issues. *Geol. Bull. China* **2008**, *27*, 1535–1550.
71. Pearce, J.A.; Harris, N.B.W.; Tindle, A.G. Trace-element discrimination diagrams for the tectonic interpretation of granitic-rocks. *J. Petrol.* **1984**, *25*, 956–983. [CrossRef]